

Fine-grained Solar Flare Forecasting Based on the Hybrid Convolutional Neural Networks*

ZHENG DENG ^{1,2,3} FENG WANG ^{1,3} HUI DENG ^{1,3} LEI TAN,¹ LINHUA DENG,⁴ AND SONG FENG²

¹Center For Astrophysics, Guangzhou University, Guangzhou 510006, P.R. China

²Faculty of Information Engineering and Automation, Kunming University of Science and Technology, Kunming 650500, P.R. China

³Great Bay Center, National Astronomical Data Center, Guangzhou, Guangdong, 510006, P.R. China

⁴Yunnan Observatories, Chinese Academy of Sciences, Kunming 650216, P.R. China

ABSTRACT

Improving the performance of solar flare forecasting is a hot topic in solar physics research field. Deep learning has been considered a promising approach to perform solar flare forecasting in recent years. We first used the Generative Adversarial Networks (GAN) technique augmenting sample data to balance samples with different flare classes. We then proposed a hybrid convolutional neural network (CNN) model (M) for forecasting flare eruption in a solar cycle. Based on this model, we further investigated the effects of the rising and declining phases for flare forecasting. Two CNN models, i.e., M_{rp} and M_{dp} , were presented to forecast solar flare eruptions in the rising phase and declining phase of solar cycle 24, respectively. A series of testing results proved: 1) Sample balance is critical for the stability of the CNN model. The augmented data generated by GAN effectively improved the stability of the forecast model. 2) For C-class, M-class, and X-class flare forecasting using Solar Dynamics Observatory (SDO) line-of-sight (LOS) magnetograms, the means of true skill statistics (TSS) score of M are 0.646, 0.653 and 0.762, which improved by 20.1%, 22.3%, 38.0% compared with previous studies. 3) It is valuable to separately model the flare forecasts in the rising and declining phases of a solar cycle. Compared with model M , the means of TSS score for No-flare, C-class, M-class, X-class flare forecasting of the M_{rp} improved by 5.9%, 9.4%, 17.9% and 13.1%, and the M_{dp} improved by 1.5%, 2.6%, 11.5% and 12.2%.

Keywords: Sun: activity – Sun: flares – techniques: image processing

1. INTRODUCTION

A solar flare is one of the most intense solar activities, manifested mainly in the sudden enhancement of the radiation flux from the radio band up to the X-rays. Flares have a significant impact on Earth's space environment, and flares also have different degrees of direct or indirect effects on meteorology and hydrology. The study of flares, especially forecasting flare eruptions, has become a research hotspot and an essential element of space weather forecasting.

As early as the 1930s, solar physicists began to forecast solar flare eruptions. Giovanelli (1939) proposed a forecast model based on the statistical relationship between flares and sunspots. Gallagher & Wang (2002) and Bloomfield et al. (2012) used the Poisson statistical model to estimate the probability of solar flares. Leka & Barnes (2003) and Barnes et al. (2007) applied the discriminant analysis to determine the significance of magnetic parameters of solar flares. By using the superimposed epoch analysis method, Mason & Hoeksema (2010) found the relationship between magnetic field parameters and solar flares.

With the rapid development of computer technology, machine learning technology was applied to the forecasting of solar flares and played an important role. For examples, the support vector machine (Yuan et al. 2010; Bobra & Couvidat 2015; Sadykov & Kosovichev 2017; Hazra et al. 2020), the artificial neural networks (Qahwaji & Colak 2007; Li & Zhu 2013; Nishizuka et al. 2018), the Bayesian network methods (Yu et al. 2010), the random forest algorithm

(Liu et al. 2017; Florios et al. 2018; Hazra et al. 2020), the ensemble learning (Colak & Qahwaji 2009), and the K-nearest neighbor (Hazra et al. 2020). Barnes et al. (2016) compared different machine learning algorithms for solar flare forecasting and demonstrated the importance of making such systematic comparisons, and of using standard verification statistics to determine what constitutes a good prediction scheme.

Deep learning neural network is a hot research topic with strong learning ability and good adaptability. It gradually develops into a mainstream technique for large-scale analysis in astrophysical research. For example, recurrent neural network (RNN) was used by many studies because it uses sequence data for training which can mine certain information such as timing information. Chen et al. (2019) adopted long short-term memory (LSTM), a special RNN, to capture both spatial and temporal information to identify the precursors of solar flare events. Wang et al. (2020) used LSTM to forecast solar flares and further investigated solar cycle dependence. Jiao et al. (2020) developed a mixed LSTM regression model to forecast the maximum solar flare intensity and found that an efficient period for forecasting the solar activity is within 24-hour before the forecasting time using the LSTM.

The convolutional neural network (CNN) (LeCun et al. 2015), a prevalent deep learning method, can automatically extract features in the field of image processing and computer vision. Compared with the classical machine learning algorithms, CNN contains several hidden layers. Each layer extracts complex features from the data before performing a classification or regression task, CNN loses less information and is more suitable for high-dimensional data.

Therefore, many research works have carried out flare forecasting using the line-of-sight magnetograms obtained by CNN on Solar Dynamics Observatory (SDO) observations. Park et al. (2018) proposed a CNN model, which is a combination of Google (Szegedy et al. 2015) and Densenet (Huang et al. 2018a), and used full-disk solar LOS magnetograms to make binary class predictions within 24 hr. Huang et al. (2018b) presented a model based on CNN for flare prediction via binary classification with 6, 12, 24, 48hr. Zheng et al. (2019) proposed a hybrid CNN model based on multi-class classification for solar flare forecast. Li et al. (2020) further developed the ability for forecasting $\geq C$ and $\geq M$ solar flares based on VGG net (Simonyan & Zisserman 2014) and Alex net (Krizhevsky et al. 2012). Their model was built on several active regions from the LOS magnetograms, the active regions selected for modeling are located within $\pm 45^\circ$ of the center of the solar disc to avoid the projection effects.

These previous studies for forecasting solar eruptions using machine learning have yielded valuable results and have played an active role in promoting space weather forecasting. However, there are still some shortcomings in the current research. Firstly, the number of samples is insufficient, especially the X-class flare samples. Secondly, all the current research work has been done for the whole solar cycle, and there is a lack of finer-grained research, such as the influence of rising and falling phases on flare forecast.

In this study, we propose and validate a more stable hybrid CNN model for forecasting flares within 24 hours in a full solar cycle. Based on this model, we further investigate the performance of fine-grained models on rising and declining phases of solar cycle 24, respectively. We introduced data preparation and data argumentation using the Generative Adversarial Networks (GAN) in Section 2. A stable CNN model for forecasting flare eruptions in a full cycle data is presented in Section 3. In Section 4, we further presented two fine-grained hybrid CNN models in the rising phase and declining phase. We discuss several issues in modeling and data analysis in Section 5. The conclusions and future works are presented in the last Section.

2. DATA PREPARATION

2.1. Data Source

Helioseismic and Magnetic Imager (HMI) is one of three instruments aboard the SDO designed to study oscillations and the magnetic field at the solar surface. HMI observes the full solar disk at 6173 Å with a resolution of 1 arc second. HMI makes two independent measurements of the LOS component of the photospheric magnetic field. One is collected every 45 seconds with the HMI Doppler camera. The other is computed every 720 seconds using filtergrams recorded by the Vector Field camera. The spatial resolution is 1 arc-second (half arc-second pixels), and the full disk images are collected on a 4096×4096 detector. The noise level is nominally between 5 and 10 Gauss.

Near the end of 2012, Space-weather HMI Active Region Patches (SHARP) data, which is convenient for AR event forecasting, were released (Bobra et al. 2014). Zheng et al. (2019) used SHARP as original data and built an excellent flare forecast model. However, many flare event records of SHARP lack location and National Oceanic and Atmospheric Administration (NOAA) active region numbers. Therefore, we use the magnetograms with a cadence of 720 seconds (hmi.M.720s) of SDO/HMI LOS magnetogram data downloaded from Joint Science Operations Center, ranging from

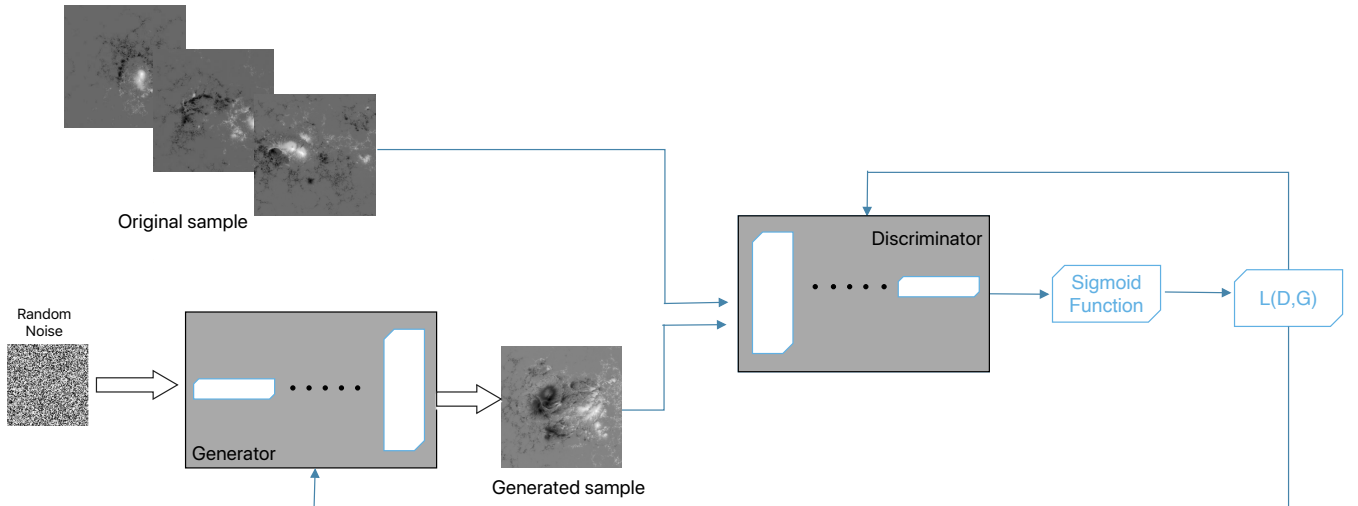


Figure 1. The training process of GAN

May 2010 to November 2019. We also select the LOS magnetograms data located within $\pm 45^\circ$ of the central meridian to decrease the projection effects (Ahmed et al. 2013; Bobra & Couvidat 2014).

Considering the data downloaded are full disk magnetograms, we collected the relevant position of active regions from <https://www.solarmonitor.org/index.php> and cut out the related section concerning solar flares with the size of 512×512 . Considering GAN and CNN require that all input images must have a fixed size, we resized all images to 128×128 images just like Zheng et al. (2019) and Li et al. (2020) did.

2.2. Data Set

To compare with the results of the previous work, especially with the results of Zheng et al. (2019), we followed strictly on the method given in the study of Zheng et al. (2019) to label the flare class with corresponding magnetograms of the active area and finally generate a data set (D) for the study. The data set D includes the magnetogram data labeled with four labels, i.e., No-flare, C-class, M-class, and X-class. The list of data volumes for each level of flare is shown in Table 1.

Table 1. The Number of Solar Magnetogram Samples We Collected

Solar Class	No-flare Class	C Class	M Class	X Class
Number	25680	13440	9120	1858

2.3. GAN And Data augmentation

Due to the significant difference in the number of samples for each flare class, we augmented the X-class samples to balance the proportion of the sample data. In general, Over-sampling is an easy method for balancing training sets that repeatedly sample the minority classes with a relatively low proportion in the training set, but over-sampling does not prevent over-fitting.

We chose GAN to augment the data. The GAN consists of two neural networks, one is the Generator (G) and the other is the Discriminator (D), which competes with each other over the available training data to improve the data quality of the generated (Goodfellow et al. 2014; Radford et al. 2015). Figure 1 shows the training process of the GAN in the study. The structures of $GNet$ and $DNet$ were designed for the GAN, respectively (see Table 2).

The input of $GNet$ is a random noise array (see Table 2), and an image with $1 \times 256 \times 256$ will be output after fully connected layers. $GNet$ contains 6 convolutional layer, we respectively chose Batch Normalization (BN) (Ioffe & Szegedy 2015) and Rectified linear unit (ReLU) (Nair & Hinton 2010) as regularization and activation function for each convolutional layer to speed up the training rate of the model and get better results.

Table 2. The structure of *GNet* and *DNet*

Layer	Type	INPUT	Kernel Size	Striding	Padding	Regularization	Activation	OUTPUT
IN	INPUT	1×2000	1×65536
FC1	Fully connected	1×65536	BN	ReLU	1×256×256
CON2	Convolution	1×256×256	5×5	1	1	BN	ReLU	64×254×254
CON3	Convolution	64×254×254	3×3	1	1	BN	ReLU	64×254×254
CON4	Convolution	64×254×254	3×3	1	1	BN	ReLU	128×128×128
CON5	Convolution	128×128×128	3×3	2	2	BN	ReLU	256×128×128
CON6	Convolution	256×128×128	3×3	1	1	BN	ReLU	128×128×128
OUT	Convolution	128×128×128	3×3	1	1	BN	ReLU	1×128×128
IN	Convolution	1×128×128	5×5	1	2	...	LeakyReLU	32×64×64
MAX2	Max-pooling	32×64×64	2×2	2	0	32×32×32
AVG3	Avg-pooling	32×32×32	2×2	2	0	32×32×32
CON4	Convolution	32×32×32	5×5	1	1	...	LeakyReLU	64×16×16
MAX5	Max-pooling	64×16×16	2×2	2	0	64×8×8
AVG6	Avg-pooling	64×8×8	2×2	2	0	64×8×8
FL7	FlattenLayer	64×8×8	1×4096
FC8	Fully connected	1×4096	LeakyReLU	1×1024
OUT	Fully connected	1×1024	Sigmoid	1×1

Table 3. The Number of Solar Magnetogram Samples of *D*

Solar Class	No-flare	C Class	M Class	X Class
Number	10272	10752	9120	9366

The sample images are first convoluted by the first convolutional layer with 5×5 kernel size. The first convolutional layer follows five convolutional layers with 3×3 kernel size.

The generated samples are further mixed with original samples and input to *DNet*. *DNet* consists of 9 layers. The first three layers contain a convolutional layer with 5×5, a max-pooling layer with 2×2, and an avg-pooling layer with 2×2 kernel size. The subsequent three layers are the same as the first three, except for the parameter of padding. The feature map obtained by convolution is output to the fully connected layer after linearization in FL7 (see Table 2). The activation function of the first fully connected layer is LeakyReLU (Maas et al. 2013) which is the same as convolutional layers. For the last activation function, we chose sigmoid (Bergstra et al. 2009) to output the judgment result.

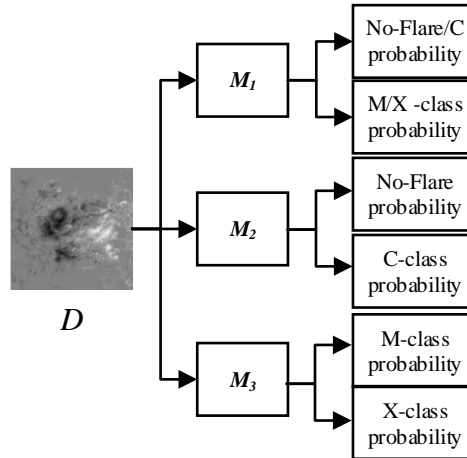
Meanwhile, the data set is undersampled by randomly selecting No-flare and C-class samples to balance the data set with about 4 samples and 8 samples per 10 samples, respectively. Finally, we generate a new data set *D* shown in Table 3. On the basis of *D*, we prepared 6 independent training sets and testing sets (see Table 4) for the subsequent modeling.

3. CNN-BASED FORECASTING MODEL WITHIN FULL SOLAR CYCLE

Referring to the model design of Alex Net (Krizhevsky et al. 2012) and VGG Net (Simonyan & Zisserman 2014), we designed a full solar cycle hybrid CNN model (*M*) for forecasting solar flare. To improve efficiency, we simplified the 4 classification problems involved in flare forecasting into 3 dichotomous problems. As shown in Table 5, the forecasting model *M* is composed of three sub-models, i.e., M_1 , M_2 and M_3 . M_1 is used to forecast M-class flares and higher levels, M_2 is used to determine whether there will be a C-class flare or not. Meanwhile, M_3 is used to identify M and X-class flare.

Table 4. The Number of Solar Magnetogram Samples of 6 Separate Data Sets

Data set	No-flare	C Class	M Class	X Class
No.1 Train	8610	8450	8200	8254
Test	939	1004	1033	948
No.2 Train	7971	8035	8080	7840
Test	1172	954	1253	948
No.3 Train	7932	7903	7847	7984
Test	1035	1253	955	948
No.4 Train	8120	8011	7987	8284
Test	1501	1093	1324	948
No.5 Train	8058	8040	8261	7947
Test	1001	1046	1378	948
No.6 Train	8129	8009	8187	7994
Test	901	1046	1124	948

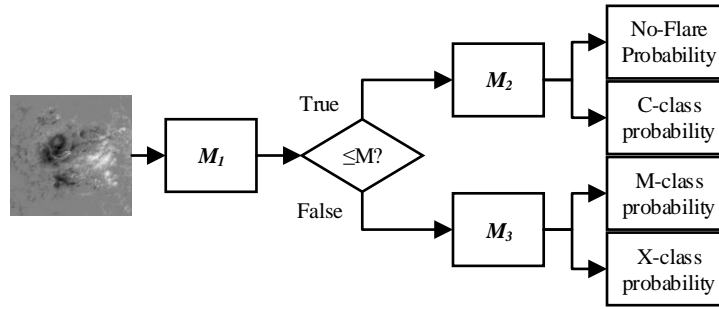
**Figure 2.** The training process of proposed hybrid CNN model

For M_1 , we designed 5 convolutional layers and 3 fully connected layers. In the first 2 convolutional layers, we used 11×11 and 5×5 kernel size respectively to convolve the main features of the image. The rest of the three convolutional layers are used to convolve detailed features. For each convolutional layer, we also chose BN and ReLU as regularization and activation. In addition, we added max-pooling with 2×2 kernel size to each of the last three convolutional layers. The feature maps obtained by convolution are multidimensional data. Therefore, it needs to be linearized before inputting to the fully connected layer. We added a layer between the convolution layer and the fully connected layer to perform linearization. For each fully connected layer, we added a Dropout (Hashemi 2012) for regularization to prevent over-fitting. We chose softmax as a classifier to output final classification results, which is often used as the last activation function of a neural network to normalize the output of a network to a probability distribution over predicted output classes.

Both M_2 and M_3 contain 3 convolutional layers with 3×3 convolution kernel to obtain detailed features and 4 fully connected layers. The parameter values of striding and padding for convolutional layers are both 1. We also added BN and ReLU for each convolutional layer. A max-pooling layer with 2×2 kernel size followed each convolutional layer. For each fully connected layer, we added a Dropout for regularization to prevent over-fitting. Classification results were output finally through by the classifier softmax as well.

Table 5. The structure of M , three models are M_1 , M_2 , M_3 from top to bottom

Layer	Type	Channel	Kernel Size	Striding	Padding	Regularization	Activation	Pooling	Output
INPUT	Convolution	1	11×11	4	1	BN	ReLU	...	64
CON2	Convolution	64	5×5	1	2	BN	ReLU	...	64
CON3	Convolution	64	3×3	1	1	BN	ReLU	Max	64
CON4	Convolution	64	3×3	1	1	BN	ReLU	Max	64
CON5	Convolution	64	3×3	1	1	BN	ReLU	Max	64
FL6	FlattenLayer	64	576
FC7	Fully Connected	576	Dropout	128
FC8	Fully Connected	128	Dropout	64
OUT	Fully Connected	64	Dropout	Softmax	...	2
INPUT	Convolution	1	3×3	1	1	BN	ReLU	Max	64
CON2	Convolution	64	3×3	1	1	BN	ReLU	Max	64
CON3	Convolution	64	3×3	1	1	BN	ReLU	Max	64
FL4	FlattenLayer	64	16384
FC5	Fully Connected	16384	Dropout	1024
FC6	Fully Connected	1024	Dropout	512
FC7	Fully Connected	512	Dropout	128
OUT	Fully Connected	128	Dropout	Softmax	...	2
INPUT	Convolution	1	3×3	1	1	BN	ReLU	Max	64
CON2	Convolution	64	3×3	1	1	BN	ReLU	Max	64
CON3	Convolution	64	3×3	1	1	BN	ReLU	Max	64
FL4	FlattenLayer	64	16384
FC5	Fully Connected	16384	Dropout	1024
FC6	Fully Connected	1024	Dropout	512
FC7	Fully Connected	512	Dropout	128
OUT	Fully Connected	128	Dropout	Softmax	...	2

**Figure 3.** The training process of proposed hybrid CNN model

The training process is shown in Figure 2. During training model M , D were input to M , M_1 is used to output the probability of flare level $\geq M$ -class flare. The training set of M_2 is a subset extracted from the training set of M_1 , including No-flare class and C-class flare samples. The role of M_2 is to forecast the probability of a C-class flare eruption. The input of M_3 is the flare data containing M-class and X-class, which is used to trained and output the probability of M-class and X-class flare.

In the process of testing, as shown in Figure 3, sample will be firstly input to the M_1 , determine whether a $\geq M$ -class flare will erupt, if judgment is True, activate M_3 , further determine whether there will be a M or X-class flare erupt

Table 6. The Training Parameter Settings of the M

Model	Learning Rate	Momentum	Batch Size	Epoch
M_1	0.001	0.5	16	50
M_2	0.001	0.7	32	50
M_3	0.001	0.7	32	50

within 24 hours. Otherwise, M_2 will be activated and the sample image will be input into M_{rp2} to determine whether there will be a C-class flare or not within 24 hours.

3.1. Optimizer for Stochastic Gradient Descent

To improve the accuracy of solar flare forecasting, we adopted the loss function based gradient descent algorithm. The core idea of the method is to minimize the loss function through training and calculate cross-entropy loss (Hinton & Salakhutdinov 2006). Pytorch provides a loss function for multi-classification problems (Ketkar 2017).

$$loss(x, \text{class}) = -\log \left(\frac{\exp(x[\text{class}])}{\sum_j \exp(x[j])} \right)$$

Based on it, we adopt the summation of the cross entropy as the loss function

$$L = \sum_{n=1}^N \sum_{k=1}^K y_{nk} \log(p(y_{nk}))$$

which greatly improved the efficiency of model training, where N represents the number of training set samples, K represents the number of the training set class, $p(y_{nk})$ and y_{nk} are the predicted output and the expected output, respectively.

We chose Adam (Kingma & Ba 2014) as the method for momentum updating. In the training process, the samples are taken as input going through the forward propagation. Then output the results of the model, and estimate the loss function L . During the backward propagation, gradients of the loss function about all weights are backpropagated through the model. Gradient descent updates the weights in the convolutional layer and the fully connected layer, and the parameters of BN to minimize the loss function at the same time. The model is repeatedly trained until the loss function L converges.

The training parameter is also crucial for achieving high predictive performance and speeding up the learning process. The parameters in our modeling are summarized in Table 6.

3.2. Model Validation

Over-fitting and under-fitting are the most common problems in CNN that could lead to erroneous forecasting results. Therefore, model validation is an indispensable part of CNN.

In the process of building M , we track the learning performance during each epoch through training loss (Train_loss) and validating loss (Val_loss). Train_loss and Val_loss are the values of the training and validation data set output by the loss function L of M for each epoch. During the learning process, Train_loss and Val_loss keep decreasing, indicating that the model is continuously learning. If Train_loss keeps decreasing while Test_loss tends to be constant, it may be that the model is over-fitting. We need to correct the model by adjusting the parameters of the convolutional layers and pooling layers. Moreover, regularization techniques could also be considered. If Train_loss tends to be constant and Test_loss keeps decreasing, there is something wrong in the dataset collation process, and we need to re-collate the dataset. If both Train_loss and Val_loss tend to remain constant, it means that the model has encountered a bottleneck in the learning process, which can be corrected by reducing the learning rate. However, if Train_loss and Test_loss keep rising simultaneously, it indicates that the network structure is unreasonable or the training hyperparameters are set improperly. The design of the model needs to be re-examined.

The relationship between Train_loss, Val_loss and epoch in the learning process of each model is shown in Figure 4. In the learning process of M_1 , we found that both Train_loss and Test_loss converge after 12 epochs. However, the Train_loss of M_2 appeared to converge after about 24 epochs, while Val_loss still experienced large fluctuations from

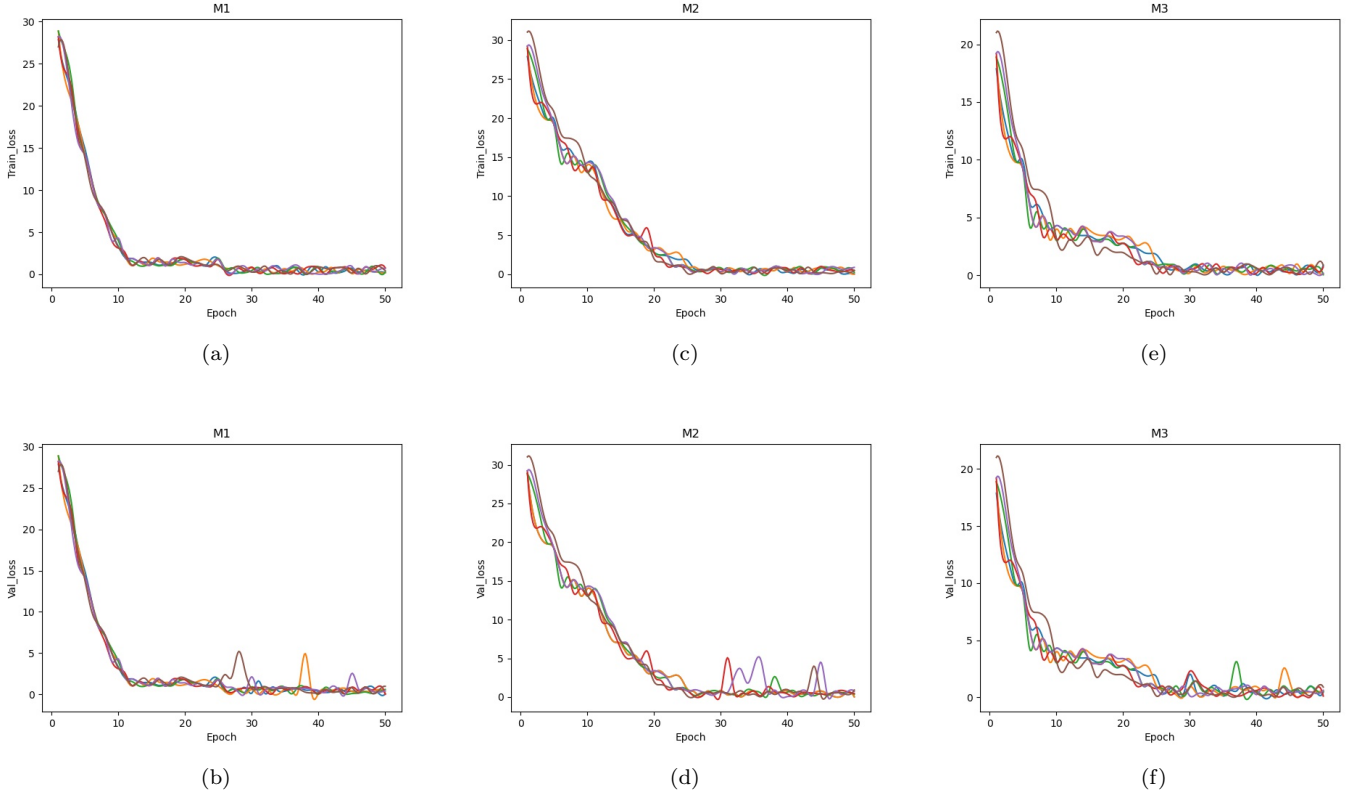


Figure 4. Learning curves showing the result of Train_loss and Val_loss per epoch for the M_1 , M_2 and M_3 . Six different color curves show the changes of Train_loss and Val_loss with epochs for the model trained and tested by six separate training and testing data sets. a and b show the result of Train_loss and Val_loss per epoch for the model M_1 , M_2 and M_3 , respectively.

the 30 to 40 epochs, which was probably caused by samples at classification thresholds. For M_3 , there is a relatively significant difference between the six different color curves for both Train_loss and Val_loss. We speculate that this is due to differences within detailed features between GAN-generated samples. However, the good thing is that all started to converge after 30 epochs. Although the relationship between Train_loss and Val_loss differs from the perfect state, it still shows that our models do not suffer from excessive over-fitting and under-fitting.

3.3. Performance Metrics

To evaluate the quality of the model, the forecast results of flare classes (No-flare, C-class, M-class and X-class) are made into a confusion matrix for evaluation. We calculated four values, i.e., True Positive (TP), True Negative (TN), False Positive (FP) and False Negative (FN), respectively.

On the basis of statistics, we further deduced several common metrics used for validating models.

- 1). Recall: the proportion of all observed True records that are forecasted to be True.

$$\text{Recall} = \frac{\text{TP}}{\text{TP} + \text{FN}}$$

- 2). Precision: The proportion of observed True in all records with True forecast.

$$\text{Precision} = \frac{\text{TP}}{\text{TP} + \text{FP}}$$

- 3). Accuracy: The proportion of correct forecasts in all records.

$$\text{Accuracy} = \frac{\text{TP} + \text{TN}}{\text{TP} + \text{FN} + \text{FP} + \text{TN}}$$

4). Heidke skill score (HSS) (Heidke 1926):

$$\text{HSS} = \frac{2[(\text{TP} \times \text{TN}) - (\text{FN} \times \text{FP})]}{(\text{TP} + \text{FN})(\text{FN} + \text{TN}) + (\text{TP} + \text{FN})(\text{FP} + \text{TN})}$$

5). True skill statistics (TSS) (Hanssen & Kuipers 1965):

$$\text{TSS} = \frac{\text{TP}}{\text{TP} + \text{FN}} - \frac{\text{FP}}{\text{FP} + \text{TN}}$$

Among these metrics, the recall, precision and accuracy all belong to the interval of $[0,1]$. When the value is equal to 1, it represents the perfect forecast of the model. Therefore, the more the value is close to 1, the more mature the model is. HSS belongs to $(-\infty,1]$ and employs the whole contingency table to quantify the accuracy of achieving correct predictions, therefore it is most frequently used in flare forecasting (Barnes & Leka 2008). The closer the value of HSS is to 1, the more accurate the forecast of the model will be. When the value of HSS is negative, we believe that metric has no reference meaning, and we need to evaluate the model with other metrics. The interval of TSS value is $[-1,1]$. When TSS value is 0, this parameter value is meaningless; when TSS value is -1, it represents the worst model; when TSS value is 1, it represents the perfect model (Woodcock 1976).

Since the TSS score is unbiased in the rate of class imbalance (Woodcock 1976), recent studies have recommended it as the primary indicator for evaluating flare forecast models (Bloomfield et al. 2012; Nishizuka et al. 2018; Zheng et al. 2019). We also followed the recommendations of Bloomfield et al. (2012), Nishizuka et al. (2018) and Zheng et al. (2019). The TSS score was used as the primary metric and the other metrics as the secondary metric in our study.

3.4. Result

After confirming that the models were well trained, we used the previous six separate testing sets to test the forecasting performance of M . The experimental results were sorted into a confusion matrix (see Table 7) to calculate the metric score of the model and paint the receiver operating characteristic (ROC) curves to compare the performance between the 3 sub-models of M . As shown in Figure 5, the AUC of M_1 , M_2 , M_3 are 0.8822, 0.8804 and 0.7956 respectively. Because pooling layer may lose some valuable information and ignore the correlation between the local and the whole, We think that the result is reasonable and expected. Meanwhile, the ACU of M_1 and M_3 are better than that of M_2 , which is consistent with the later experimental results. In general, M_1 and M_3 are more stable and efficient than M_2 .

The means and standard deviations of these forecasting results are also presented in Table 8. M has TSS scores of 0.757 ± 0.033 , 0.646 ± 0.060 , 0.653 ± 0.078 , 0.762 ± 0.018 for No-flare, C-class, M-class, and X-class flare forecasting, respectively. Except for No-flare, the average of the TSS of C-class, M-class and X-class are significantly better than those of Zheng et al. (2019). The mean TSS of No-flare obtained from our model is 0.757 which is slightly lower than 0.768 of Zheng et al. (2019).

In addition, for M and X-class flare forecasting, the means of the TSS scores are higher than the highest values 0.653, 0.740 of Zheng et al. (2019) and Bloomfield et al. (2012) respectively. Moreover, the standard deviations are 0.078 and 0.018, respectively, which are much lower than 0.137 and 0.370 of Zheng et al. (2019). It means that our model is more robust than that of Zheng et al. (2019).

Meanwhile, the sub-model M_1 has a good performance for the binary classification task (\geq M-class flare forecasting). The best and the worst TSS score, calculated from the confusion matrix in Table 7, are 0.830 and 0.718 for \geq M-class flare forecasting, respectively. The scores are better than 0.800 of Chen et al. (2019), 0.539 of Bloomfield et al. (2012), and 0.774 (mean of TSS score) of Li et al. (2020). Moreover, the standard deviation of the sub-model M_1 is 0.056, which is also lower than 0.079 of Li et al. (2020).

4. FINE-GRAINED HYBRID CNN MODEL

A solar cycle consists of rising and declining periods, and there is some difference in the intensity of solar activity between the rising and declining periods. After modeling solar flare forecasting within a full-cycle, we realized that this difference might have some implications for model building. This section further investigates the independent modeling of the rising and declining phases separately and evaluates their performance.

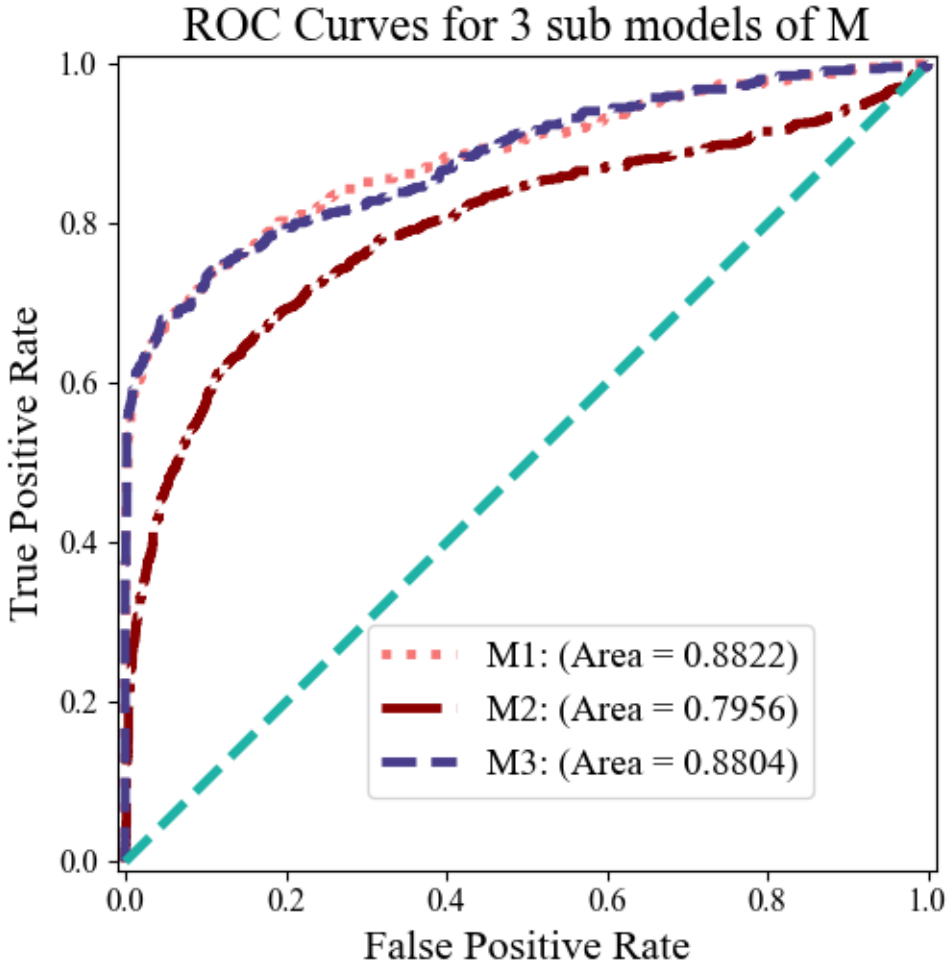


Figure 5. The ROC Curves and AUC(the Area) of 3 sub models of M

4.1. Data Set Preparation

We continued to use the dataset D on which the model M was built. We divide the dataset D into D_{rp} and D_{dp} . The D_{rp} is the subset of the rising phase (T_{rp}) in the solar cycle 24 from May 2010 to April 2014. D_{dp} is the subset of the declining phase (T_{dp}) from May 2014 to November 2019.

4.2. Modeling For Rising and Declining Phases

Two hybrid CNN models (M_{rp} and M_{dp}) are built for rising and declining phases, respectively. M_{dp} is the same as M . However, there is a certain difference between M_{rp} and M . M_{rp} also contains 3 CNN model, i.e., M_{rp1} , M_{rp2} and M_{rp3} . However, we modified the convolution kernels of the first two convolutional layers to 15×15 and 11×11 compared to M_1 for M_{rp1} . As for M_{rp2} and M_{rp3} , we added a layer after CON3 (see Table 5) which is the same as CON3, and removed a fully connected layer. The specific modeling and tuning process is similar to the previous modeling and tuning of M .

It is necessary to note that there is not much objective basis for such a model change. We finally built this model through extensive tuning and testing. The modification of the model may be caused by the different characteristics of the magnetic fields in the rising and declining phases. Solar flare releases its energy previously stored in the magnetic field, which is a rapid transformation process of magnetic energy of the solar active regions into the kinetic energy of plasma flow, particle, radiation, and heat. As the duration of the rising phase is shorter than the declining phase of a

Table 7. The values of the confusion matrix of M on Each of 6 Data Sets

Observation ↓ Prediction →	No-flare Class	C Class	M Class	X Class
No.1: No-flare	824	134	20	2
C Class	154	768	69	30
M Class	2	133	888	131
X Class	1	66	69	747
No.2: No-flare	817	126	27	1
C Class	154	744	161	23
M Class	103	122	789	118
X Class	0	64	162	768
No.3: No-flare	920	115	27	0
C Class	158	820	32	24
M Class	38	66	729	134
X Class	5	24	257	752
No.4: No-flare	713	135	4	13
C Class	136	800	125	61
M Class	3	115	980	225
X Class	2	4	122	859
No.5: No-flare	809	147	10	21
C Class	41	889	104	47
M Class	4	13	810	139
X Class	0	5	117	751
No.6: No-flare	613	117	4	0
C Class	163	829	130	0
M Class	103	88	590	228
X Class	2	20	197	765

solar cycle, that is to say, the physical process of flare energy storage and dissipation in the two phases may exhibit different spatio-temporal behaviors (Hudson 2011).

4.3. Results of M_{rp} and M_{dp}

Precisely as in the previous sections, we evaluated the performance of M_{rp} and M_{dp} , still mainly on the TSS.

First of all, we input the sub testing sets of D into the M_{rp} and M_{dp} , respectively, and make the output results of the model into Table 9 and Table 10 according to the confusion matrix. Then calculate the mean and standard deviation for each solar flare class forecast, which is recorded with M in Table 11.

According to Table 11, all model evaluation metrics of M_{rp} are better than M in the flare forecast of No-flare, C, M and X-class. The TSS score of M_{rp} , they are up to 0.802 ± 0.013 , 0.707 ± 0.018 , 0.770 ± 0.042 and 0.862 ± 0.064 , respectively. Meanwhile, the TSS score of M_{dp} for No-flare, C-class, M-class, and X-class were better than M , which were 0.768 ± 0.036 , 0.663 ± 0.032 , 0.728 ± 0.039 and 0.855 ± 0.007 . However, for the No-flare and C-class flares forecast, the difference of mean between M and M_{dp} is only 0.012 and 0.017. We realized this is a reasonable result caused by the same model structure. However, in the forecasting of M and X-class, the TSS score has greatly improved by 17.9%, 13.1%. Combined with the forecast result of M_{rp} , it proved that investigating the modeling for the rising phase and the declining phase is an effective method to improve the accuracy of forecasting solar flare.

5. DISCUSSIONS

5.1. Augmented Data Validation

Table 8. The Flare Prediction Results (within 24 hr) of M and Comparison with Previous Studies.

Metric	Model	No-flare Class	C Class	M Class	X Class	$\geq M$ Class(M_1)
Recall	M	0.806±0.034	0.734±0.047	0.746±0.072	0.830±0.010	0.890±0.041
	Chen et al. (2019)	0.930
	Zheng et al. (2019)	0.869±0.034	0.671±0.059	0.617±0.148	0.594±0.394	...
	Li et al. (2020)	0.817±0.084
	Bloomfield et al. (2012)	...	0.737	0.693	0.859	0.704
Precision	M	0.849±0.012	0.744±0.044	0.740±0.031	0.780±0.050	0.907±0.029
	Chen et al. (2019)	0.870
	Zheng et al. (2019)	0.793±0.054	0.670±0.079	0.699±0.087	0.562±0.383	...
	Li et al. (2020)	0.889±0.056
	Bloomfield et al. (2012)	0.136	0.029	0.146
Accuracy	M	0.913±0.008	0.865±0.023	0.864±0.024	0.909±0.014	0.886±0.029
	Chen et al. (2019)
	Zheng et al. (2019)	0.891±0.018	0.812±0.029	0.849±0.034	0.933±0.041	...
	Li et al. (2020)	0.891±0.024
	Bloomfield et al. (2012)	...	0.711	0.829	0.881	0.830
HSS	M	0.751±0.038	0.644±0.062	0.655±0.085	0.770±0.013	0.764±0.071
	Chen et al. (2019)	0.810
	Zheng et al. (2019)	0.747±0.037	0.535±0.061	0.551±0.120	0.539±0.366	...
	Li et al. (2020)	0.759±0.071
	Bloomfield et al. (2012)	0.136	0.029	0.190
TSS	M	0.757±0.033	0.646±0.060	0.653±0.078	0.762±0.018	0.774±0.056
	Chen et al. (2019)	0.800
	Zheng et al. (2019)	0.768±0.028	0.538±0.059	0.534±0.137	0.552±0.370	...
	Li et al. (2020)	0.749±0.079
	Bloomfield et al. (2012)	...	0.443	0.526	0.740	0.539
TSS Rate	Chen et al. (2019)	-3.3%
Improved	Zheng et al. (2019)	-1.4%	20.1%	22.3%	38.0%	...
	Li et al. (2020)	3.3%
	Bloomfield et al. (2012)	...	45.8%	24.1%	3.0%	43.6%

The number of different samples required in machine learning is balanced. The trustworthiness of the data added by GAN is a basis for the whole research work.

To validate the samples augmented by the GAN, we use the X-class samples augmented by GAN as the training data and the original X-class samples as the testing data for model M .

Firstly, We chose two training sets, i.e., the generated X samples and the original X samples, to train M and then use the rest of the original sample to test. 801 out of 968 X-class samples were identified with X-class sample data augmented, 711 out of 846 samples were misidentified without X-class sample data augmented (see Table 12). We found that the result of M is very unsatisfactory due to too few original samples of X-class, but it has been apparently improved after using GAN to augment the number of X-class samples. Therefore, we realized that: 1) Too few samples of X-class directly impact the quality of the model. 2) The X-class samples generated by GAN are reliable and can be used as the training set of M .

5.2. The Implications of Three Models

Table 9. Values of confusion matrix for testing M_{rp} on each of 6 Data Sets

Observation↓ Prediction→	No-flare	C Class	M Class	X Class
No.1: No-flare	782	134	0	7
C Class	133	805	88	16
M Class	18	60	887	31
X Class	6	5	58	894
No.2: No-flare	965	59	1	1
C Class	121	747	58	15
M Class	82	91	853	34
X Class	4	57	104	898
No.3: No-flare	903	168	1	0
C Class	116	927	33	23
M Class	14	108	759	129
X Class	2	50	162	796
No.4: No-flare	1337	44	3	5
C Class	109	777	176	21
M Class	28	248	1004	32
X Class	27	24	141	890
No.5: No-flare	857	163	67	2
C Class	104	825	183	9
M Class	20	39	986	28
X Class	20	19	142	909
No.6: No-flare	766	140	0	0
C Class	88	854	81	3
M Class	26	42	868	45
X Class	21	10	175	900

In the study, we built a hybrid CNN model (M) for forecasting solar flares within 24 hours in a full solar cycle. Then we built M_{rp} and M_{dp} for the rising and declining phase by using the samples in different phases. All three models achieved reliable forecasting results for their periods.

However, from the modeling point of view, the model structure of M and M_{dp} is basically the same. M_{rp} increases the number of layers and modifies the kernel size on top of M , which raises a question worth discussing whether M_{rp} is a more accurate predictor of flares occurring over the full solar cycle. We have tried to use M_{rp} to forecast solar flares in T , the means of TSS score are not ideal, which are 0.470, 0.312, 0.549, 0.642 for No-flare, C-class, M-class, X-class flare forecasting, respectively.

Therefore, we believe that the three models have their own forecasting significance in their own periods. When we cannot identify the period which the sample belongs to, we can use M to forecast. Conversely, we use the corresponding model to forecast.

6. CONCLUSIONS AND FUTURE WORK

In the study, we first augmented the X-class samples using the GAN and then divided the augmented X samples and real samples into the training and testing sets, respectively. Then balanced the proportion of samples in each category by using other methods such as under-sampling. After organizing the dataset, we proposed a hybrid convolutional neural network model (M) for forecasting flare eruption in a solar cycle. Basing on this model, we further investigated the effects of the rising and declining phases for flare forecasting. Two-hybrid CNN models, i.e., M_{rp} and M_{dp} , were presented to forecast solar flare eruption in the rising phase and declining phase of the solar cycle, respectively.

Table 10. Values of confusion matrix for testing M_{dp} on each of 6 Data Sets

Observation↓ Prediction→	No-flare	C Class	M Class	X Class
No.1: No-flare	849	179	0	0
C Class	174	750	84	41
M Class	63	33	796	71
X Class	0	0	68	836
No.2: No-flare	887	115	20	0
C Class	132	800	149	42
M Class	60	192	916	67
X Class	0	2	61	801
No.3: No-flare	493	32	0	0
C Class	91	492	55	0
M Class	10	92	417	30
X Class	0	0	52	210
No.4: No-flare	1056	40	8	33
C Class	298	961	112	9
M Class	126	79	873	38
X Class	21	13	85	830
No.5: No-flare	909	19	32	0
C Class	286	968	206	0
M Class	33	143	915	38
X Class	19	6	164	872
No.6: No-flare	1058	79	9	0
C Class	287	861	90	2
M Class	131	113	1082	7
X Class	25	40	97	901

Overall, all three flare forecasting models developed in this study have excellent accuracy and stability. Significantly, the accuracy of the two models for the rising and declining phases is more advantageous, which provides a more reliable means to carry out space weather forecasting in the later stage.

This work is supported by the National SKA Program of China (2020SKA0110300), the Joint Research Fund in Astronomy (U1831204, U1931141) under cooperative agreement between the National Natural Science Foundation of China (NSFC) and the Chinese Academy of Sciences (CAS), the Funds for International Cooperation and Exchange of the National Natural Science Foundation of China (11961141001). This work is also supported by Astronomical Big Data Joint Research Center, co-founded by National Astronomical Observatories, Chinese Academy of Sciences and Alibaba Cloud.

Thanks to SDO and NASA for the data and data information.

The authors gratefully acknowledge the helpful comments and suggestions of the reviewers.

REFERENCES

- Ahmed, O. W., Qahwaji, R., Colak, T., et al. 2013, *Solar Physics*, 283, 157
- Barnes, G., & Leka, K. 2008, *The Astrophysical Journal Letters*, 688, L107
- Barnes, G., Leka, K. D., Schumer, E. A., & Della-Rose, D. J. 2007, *Space Weather*, 5, 9002
- Barnes, G., Leka, K., Schrijver, C., et al. 2016, *The Astrophysical Journal*, 829, 89

Table 11. The flare forecasting results (within 24 hours) of M_{rp} and M_{dp}

Metric	Model	No-flare Class	C Class	M Class	X Class
Recall	M	0.806±0.034	0.734±0.047	0.746±0.072	0.830±0.010
	M_{rp}	0.842±0.021	0.774±0.026	0.830±0.027	0.910±0.050
	M_{dp}	0.811±0.021	0.766±0.033	0.811±0.020	0.879±0.003
Precision	M	0.849±0.012	0.744±0.044	0.740±0.031	0.780±0.050
	M_{rp}	0.876±0.045	0.802±0.030	0.815±0.057	0.853±0.058
	M_{dp}	0.877±0.047	0.732±0.027	0.775±0.037	0.884±0.059
Accuracy	M	0.913±0.008	0.865±0.023	0.864±0.024	0.909±0.014
	M_{rp}	0.929±0.004	0.890±0.008	0.912±0.017	0.942±0.023
	M_{dp}	0.916±0.016	0.861±0.008	0.889±0.021	0.957±0.002
HSS	M	0.751±0.038	0.644±0.062	0.655±0.085	0.770±0.013
	M_{rp}	0.796±0.019	0.702±0.028	0.772±0.037	0.871±0.064
	M_{dp}	0.757±0.033	0.668±0.035	0.734±0.036	0.852±0.002
TSS	M	0.757±0.033	0.646±0.060	0.653±0.078	0.762±0.018
	M_{rp}	0.802±0.013	0.707±0.018	0.770±0.042	0.862±0.064
	M_{dp}	0.768±0.036	0.663±0.032	0.728±0.039	0.855±0.007
TSS (Mean)	M_{rp}	5.9%	9.4%	17.9%	13.1%
improved over M	M_{dp}	1.5%	2.6%	11.5%	12.2%

Table 12. The confusion matrix of M with and without X-class sample data augmented from left to right

Observation↓ Prediction→			Observation↓ Prediction→		
Others	X-Class		Others	X-Class	
Others	887	167	Others	835	711
X-Class	132	801	X-Class	126	136

- Bergstra, J., Desjardins, G., Lamblin, P., & Bengio, Y. 2009, Technical report, 1337
- Bloomfield, D. S., Higgins, P. A., Mcateer, R., & Gallagher, P. T. 2012, The Astrophysical Journal Letters, 747
- Bobra, M. G., & Couvidat, S. 2014, Astrophysical Journal, 798, 135
- . 2015, The Astrophysical Journal, 798, 135
- Bobra, M. G., Sun, X., Hoeksema, J. T., et al. 2014, Solar Physics, 289, 3549
- Chen, Y., Manchester, W. B., Hero, A. O., et al. 2019, Space Weather, 17, 1404
- Colak, T., & Qahwaji, R. 2009, Space Weather, 7
- Florios, K., Kontogiannis, I., Park, S. H., et al. 2018, Solar Physics, 293, 1
- Gallagher, P. T., & Wang, M. H. 2002, Solar Physics
- Giovanelli, R. G. 1939, The Astrophysical Journal, 89, 555
- Goodfellow, I. J., Pouget-Abadie, J., Mirza, M., et al. 2014, Generative Adversarial Networks. <https://arxiv.org/abs/1406.2661>
- Hanssen, A., & Kuipers, W. 1965, On the Relationship Between the Frequency of Rain and Various Meteorological Parameters: (with Reference to the Problem of Objective Forecasting), Koninkl. Nederlands Meteorologisch Instituut. Mededelingen en Verhandelingen (Staatsdrukkerij- en Uitgeverijbedrijf). <https://books.google.co.kr/books?id=nTZ8OgAACAAJ>
- Hashemi, H. 2012, IEEE Signal Processing Magazine, 29, 82, doi: 10.1109/MSP.2012.2185897
- Hazra, S., Sardar, G., & Chowdhury, P. 2020, Astronomy & Astrophysics, 639, A44
- Heidke, P. 1926, Geografiska Annaler, 8, 301
- Hinton, G. E., & Salakhutdinov, R. R. 2006, science, 313, 504
- Huang, X., Wang, H., Xu, L., et al. 2018a, Astrophysical Journal, 856, 7
- . 2018b, The Astrophysical Journal, 856, 7
- Hudson, H. S. 2011, Space Science Reviews, 158, 5

- Ioffe, S., & Szegedy, C. 2015, CoRR, abs/1502.03167.
<https://arxiv.org/abs/1502.03167>
- Jiao, Z., Sun, H., Wang, X., et al. 2020, *Space Weather*, 18, e2020SW002440
- Ketkar, N. 2017, in *Deep learning with python* (Springer), 195–208
- Kingma, D. P., & Ba, J. 2014, arXiv preprint arXiv:1412.6980
- Krizhevsky, A., Sutskever, I., & Hinton, G. E. 2012, *Advances in neural information processing systems*, 25, 1097
- LeCun, Y., Bengio, Y., & Hinton, G. 2015, *nature*, 521, 436
- Leka, K., & Barnes, G. 2003, *The Astrophysical Journal*, 595, 1296
- Li, R., & Zhu, J. 2013, *Research in Astronomy and Astrophysics*, 13, 1118
- Li, X., Zheng, Y., Wang, X., & Wang, L. 2020, *The Astrophysical Journal*, 891, 10
- Liu, C., Deng, N., Wang, J. T., & Wang, H. 2017, *The Astrophysical Journal*, 843, 104
- Maas, A. L., Hannun, A. Y., Ng, A. Y., et al. 2013 in , Citeseer, 3
- Mason, J. P., & Hoeksema, J. 2010, *The Astrophysical Journal*, 723, 634
- Nair, V., & Hinton, G. E. 2010, in *Proceedings of the 27th International Conference on International Conference on Machine Learning, ICML'10* (Madison, WI, USA: Omnipress), 807–814
- Nishizuka, N., Sugiura, K., Kubo, Y., Den, M., & Ishii, M. 2018, *The Astrophysical Journal*, 858, 113
- Park, E., Moon, Y.-J., Shin, S., et al. 2018, *The Astrophysical Journal*, 869, 91
- Qahwaji, R., & Colak, T. 2007, *Solar Physics*, 241, 195
- Radford, A., Metz, L., & Chintala, S. 2015, arXiv preprint arXiv:1511.06434
- Sadykov, V. M., & Kosovichev, A. G. 2017, *The Astrophysical Journal*, 849, 148
- Simonyan, K., & Zisserman, A. 2014, arXiv preprint arXiv:1409.1556
- Szegedy, C., Liu, W., Jia, Y., et al. 2015, in *Proceedings of the IEEE conference on computer vision and pattern recognition*, 1–9
- Wang, X., Chen, Y., Toth, G., et al. 2020, *The Astrophysical Journal*, 895, 3
- Woodcock, F. 1976, *Monthly Weather Review*, 104, 1209
- Yu, D., Huang, X., Wang, H., et al. 2010, *The Astrophysical Journal*, 710, 869
- Yuan, Y., Shih, F. Y., Jing, J., & Wang, H.-M. 2010, *Research in Astronomy and Astrophysics*, 10, 785
- Zheng, Y., Li, X., & Wang, X. 2019, *The Astrophysical Journal*, 885, 73